VPS VIBRATIONS IN PHYSICAL SYSTEMS

DOI: 10.21008/j.0860-6897.2026.1.04
Vibrations in Physical Systems, 2026, 37(1), 2026104

Defect detection in MAG welding using multi-sensor wavelet scattering features and deep autoencoders

Solomon Habtamu TESSAMA, **Dariusz BISMOR**

Faculty of Automatic Control, Electronics and Computer Science, Department of Measurements and Control Systems, Silesian University of Technology, 44-100 Gliwice, Poland

Corresponding author: Solomon Tessema, stessema@polsl.pl

Abstract This paper presents an automated defect detection system for Metal Active Gas (MAG) welding, designed to improve the speed and reliability of welding. Defects can significantly compromise welding joint quality. The proposed system uses data collected from microphones, vibration sensors, and photodiodes during welding. These signals are processed using wavelet scattering transforms to extract features that capture the underlying patterns of the welding process. The resulting scattering coefficients are organized into vectors and fed into a deep autoencoder trained exclusively on defect-free welded joints. Defects are detected based on mean squared error, with an optimal threshold selected to clearly separate defect-free ("Good") joints from defective ones by maximizing the F1 score. Since the model has not seen defective data during training, it produces higher errors when processing flawed welded joints, allowing for effective unsupervised defect detection. Comparative evaluation with supervised models indicates that SVM achieves 95.9% accuracy, 95.9% F1 score, and 99.5% ROC AUC with SMOTE-based balancing, while 1D CNN achieves 96.9% accuracy, 96.9% F1 score, and 99.9% ROC AUC with SMOTE. In contrast, the deep autoencoder demonstrates superior performance with 98.1% accuracy, 98.3% F1 score, and 99.7% ROC AUC without requiring labeled defect data or class balancing. These results highlight the effectiveness of the proposed unsupervised framework as a robust and scalable solution for defect detection in highly imbalanced welding datasets.

Keywords: MAG welding, defect detection, wavelet scattering transform, deep autoencoder.

1. Introduction

Defect detection in welding processes has been the focus of significant research, particularly as manufacturers seek more reliable and automated methods for quality assurance. In Metal Active Gas (MAG) welding, defects such as porosity, spatter, and lack of fusion can compromise structural integrity [1–3]. Traditional inspection methods, including visual checks, X-ray imaging, and ultrasonic testing are often time-consuming, subjective, and expensive, making them less suitable for real-time monitoring in high-throughput environments [4, 5].

Recent studies have explored the use of sensor-based monitoring to detect welding anomalies. Acoustic signals, vibration measurements, and photodiode outputs have all been used to capture the dynamic behavior of the welding process. For example, [6] demonstrated that microphone and accelerometer data can effectively identify spatter events, while [7] employed photodiode signals to detect arc instability.

Feature extraction remains a critical step in translating raw sensor data into meaningful indicators of weld quality [8]. Conventional signal-processing techniques, such as FFT or short-time Fourier transforms, often struggle with the non-stationary nature of welding signals. Wavelet transforms have gained popularity due to their ability to localize both time and frequency information [9]. More recently, wavelet scattering transforms have emerged as a more stable and interpretable approach, offering improved invariance to small deformations and noise [10,11].

On the machine-learning front, supervised models such as SVMs, and CNNs have been applied to classify welding defects [7]. However, these methods require large, well-labeled datasets that are often difficult to obtain in industrial settings. This challenge has driven growing interest in unsupervised approaches [9,12, 13]. Autoencoders have proven effective for anomaly detection by learning to reconstruct normal samples and flagging those with high reconstruction errors. Studies in [14, 15] have applied deep autoencoders to welding quality inspection, though typically using single-sensor inputs or limited feature engineering.

More recent work indicates that unsupervised multi-sensor approaches can further improve defect detection in manufacturing. Vibration analysis using unsupervised algorithms can reveal system anomalies [16, 17], while acoustic–visual fusion has been shown to enhance defect detection in GMAW compared with single-sensor methods [10, 18]. Wavelet-based acoustic signatures effectively capture transient melt-pool dynamics in DED-Arc processes [18, 19], and wavelet–autoencoder models provide compact features for high-rate, unlabeled sensor data [17, 19]. Collectively, these studies demonstrate that multi-sensor fusion combined with wavelet-enhanced deep representations is highly effective for real-time, unsupervised defect detection.

Despite these advances, research on combining wavelet scattering features with multi-sensor data in an unsupervised framework remains limited. Integrating multimodal signals improves robustness, while wavelet scattering offers stable and informative features [11,13]. When coupled with a deep autoencoder trained on defect-free data, this approach enables accurate, real-time defect detection without requiring labeled datasets [8,9,12].

2. Experimental configuration for MAG welding

MAG welding uses consumable electrode and shielding gas to improve weld quality. As shown in Figure 1, the electrode supplies filler material while the shielding gas protects the weld pool from atmospheric contamination. Data acquisition is performed through a National Instruments CompactDAQ system that connects the sensors to a computer. The sensor enclosure contains MEMS and electret microphones as well as photodiodes, while a GRAS microphone is mounted on the top surface. In this study, an electret microphone, photodiodes, and an ADXL386 accelerometer are used to monitor the MAG welding process. The microphone records acoustic signatures to identify arc-related anomalies [20]; the accelerometer measures vibration to assess mechanical behavior; and the photodiodes track arc light intensity to provide additional insight into welding stability [5, 21, 22].

3. Wavelet scattering feature extraction

The wavelet scattering transform is a nonlinear signal representation method that combines multiscale wavelet analysis with modulus nonlinearities and low-pass filtering. The transform extracts stable, translation-invariant features from signals while preserving high-frequency information typically lost during standard averaging [10,11]. Traditional wavelet transforms are good at capturing localized frequency information but are not stable under small translations or deformations. The scattering transforms addresses this by cascading wavelet convolutions, modulus operations, and low-pass filtering, which together produce a hierarchy of coefficients encoding the geometric structure of the signal [11,13]. The scattering transform constructs a sequence of coefficients using wavelet convolutions followed by nonlinearity and averaging. The zero-order coefficient is simply the signal averaged with a low-pass filter ϕ_J:

$$S_0\tilde{x}(t) = \tilde{x} * \phi_J\,(t). \tag{1}$$

where $S_0\tilde{x}(t)$is the zeroth-order scattering coefficient, representing the coarse or average behavior of the signal and obtained by averaging input time-domain signal $\tilde{x}$ with the low-pass filter $\phi_J(t)$. Here, $*$ denotes the convolution operation.

To compute the first-order coefficients, the signal is convolved with a wavelet filter, passed through a modulus, and averaged:

$$U_1(t,\ \lambda_1) = |\tilde{x} * \psi\lambda_1(t)|\,, \tag{2}$$

where $U_1(t,\lambda_1)$is the first-order propagated coefficient, $\psi_{\lambda_1}(t)$is the wavelet filter at scale λ_1, $\lambda_1$denotes the first wavelet scale, and $|\cdot|$ denotes the modulus (absolute value) operator.

$$S_1(t,\ \lambda_1) = U_1(\cdot,\ \lambda_1) * \phi_J\ (t), \tag{3}$$

where $S_1(t,\lambda_1)$is the first-order scattering coefficient, $U_1(\cdot,\lambda_1)$is the first-order propagated coefficient, $\phi_J(t)$is the low-pass filter used for averaging, and $(\cdot)$ is a placeholder indicating the variable over which convolution is performed.

Second-order coefficients are built by applying the same process to the first-order output:

$$U_2(t,\ \lambda_1,\ \lambda_2) = |U_1(\cdot,\lambda_1) * \psi\lambda_2(t)|\,, \tag{4}$$

where $U_2(t,\lambda_1,\lambda_2)$is the second-order propagated coefficient, $U_1(\cdot,\lambda_1)$is the first-order propagated coefficient, $\psi_{\lambda_2}(t)$is the second wavelet filter, $\lambda_2$denotes the second wavelet scale, and (λ_1, λ_2)defines the scattering path.

$$S_2(t,\ \lambda_1,\ \lambda_2) = U_2(\cdot,\ \lambda_1,\ \lambda_2) * \phi_J(t), \tag{5}$$

where $S_2(t,\lambda_1,\lambda_2)$is the second-order scattering coefficient obtained by averaging the second-order propagated coefficient $U_2(t, \lambda_1, \lambda_2)$.

Higher-order coefficients can be defined in the same way, though in practice, orders up to 2 are often sufficient for most applications. Before computing the scattering transform, input signals are standardized and adjusted to a fixed length. If the raw signal x_{raw} has fewer than L samples, it is zero-padded. If longer, it is truncated [11]:

$$x = \begin{cases} [x_{raw};\ 0_{L-N}], & N < L, \\ x_{raw}\ [1:\ L], & N \geq L. \end{cases} \tag{6}$$

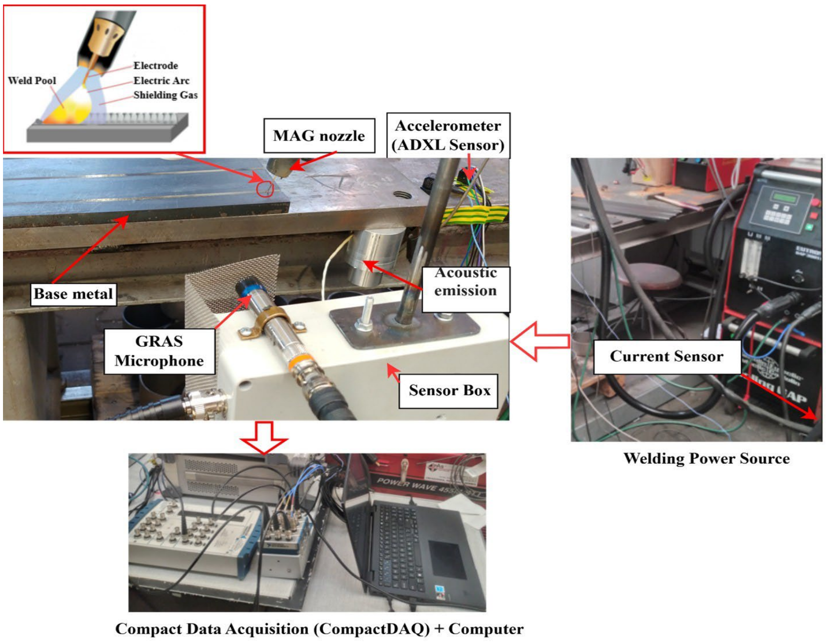

Figure 1. Experimental Welding Setup.

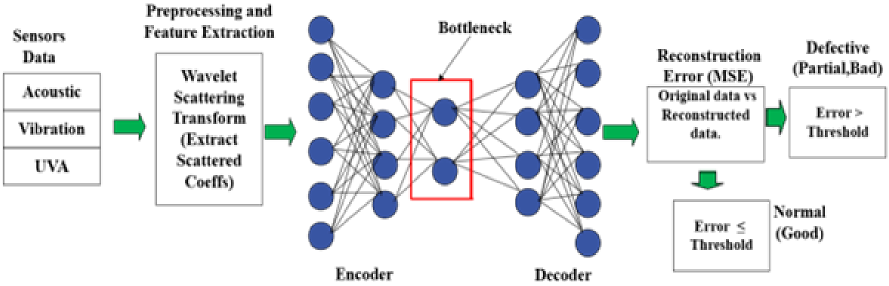

Figure 2. Deep autoencoder framework for defect detection.

The signal is then normalized to have zero mean and unit variance:

$$\tilde{X} = \frac{x - \mu_x}{\sigma_x + \varepsilon}, \tag{7}$$

where μ_x is the mean, σ_x is the standard deviation, and ε is a small constant for numerical stability.
After computing the scattering coefficients, they are averaged and concatenated to form a feature vector:

$$\mathbf{f} = \mathrm{vec}(\{s_0, s_1(\lambda_1), s_2(\lambda_1, \lambda_2)\}) \epsilon R^d. \tag{8}$$

This vector captures multi-resolution, hierarchical information from the signal and is suitable for downstream tasks like classification or regression.

3.1. Parameter settings

The scattering transform is typically configured with the following parameters: signal length L = 1024, sampling frequency fs = 25.6 kHz, invariance scale T (which defines the low-pass filter scale), quality factors Q = [2, 1] (which control the wavelet filter bandwidths), and an oversampling factor of 2 (controlling the temporal resolution of the coefficients). The temporal averaging parameter Tin the wavelet scattering transform defines the effective low-pass window applied to the scattering coefficients. For 1024-sample segments ($fs = 25.6$ kHz, corresponding to approximately 0.04 s), Tcontrols the trade-off between temporal resolution and smoothing: smaller values preserve short-term variations and enhance sensitivity to transient anomalies, while larger values increase smoothing, potentially masking brief defect signatures.

4. Autoencoder-Based defect detection

An autoencoder is a type of artificial neural network used for unsupervised learning, particularly for tasks involving dimensionality reduction and anomaly detection. It consists of two primary components: an encoder that compresses the input into a lower-dimensional latent representation and a decoder that attempts to reconstruct the original input from this compressed form [12]. The learning objective is to minimise the reconstruction loss, typically quantified using the MSE between the input vector $x \varepsilon R^n$ and its reconstruction $\hat{x}$. Mathematically, the loss function is expressed as:

$$L(x,\ \hat{x}) = \frac{1}{n}\sum_{i=1}^{n}(x_i - \hat{x}_i)^2. \tag{9}$$

The encoder maps the input to the latent space using a nonlinear transformation:

$$z = \phi(w_{ex} + b_e), \tag{10}$$

while the decoder reconstructs the input via:

$$\hat{x} = \phi(w_{dz} + b_d), \tag{11}$$

where w_{ex}, w_{dz} are weight matrices, b_e, b_d are bias vectors, and ϕ is an activation function.

Autoencoders are well-suited for defect detection when trained exclusively on normal data, such as inputs from the" Good" class. In this setting, the model learns to accurately reconstruct normal samples but performs poorly on defective ones, resulting in higher reconstruction errors. A defect score is computed based on this error, and inputs are classified as defective if the reconstruction loss satisfies L(x, $\hat{x}$) > τ, where L(x, $\hat{x}$)is the loss between the input x and its reconstruction $\hat{x}$, and τ is a predefined threshold [17,19].

4.1. Threshold optimization

To distinguish defective data points from normal ones based on the mean squared error (MSE), the optimal threshold is determined by maximizing the F1 score [8,9]. First, precision (P) and recall (R) are computed across a range of MSE thresholds using the precision–recall curve. Precision and recall are defined as:

$$P = \frac{TP}{TP+FP},\ R = \frac{TP}{TP+FN}. \tag{12}$$

Here, TP, FP , and FN represent the counts of true positives, false positives, and false negatives, respectively. For each candidate threshold τ , the F1 score is calculated as the harmonic mean of precision and recall:

$$F1(\tau) = 2 \cdot \frac{P(\tau) * R(\tau)}{P(\tau) + R(\tau)}. \tag{13}$$

The threshold τ^* that maximizes the F1 score is selected as the optimal cutoff:

$$\tau^* = \arg\max F1(\tau). \tag{14}$$

This method ensures an optimal balance between precision and recall, which is especially important in defect detection where false positives and false negatives have significant implications [8].

4.2. Dataset description

The dataset contains 955 samples from MAG welding sessions, segmented into 1-second intervals and labeled as "Good," "Bad," and "Partial" by experts, with 594, 327, and 34 samples in each class, respectively. Only the Good samples were used to train the autoencoder. Standard k-fold cross-validation is not employed, as the model is unsupervised. A separate validation set of Good and Partial segments is used to tune the threshold, while testing is performed on all classes to evaluate defect detection. In contrast, SVM and 1D CNN models are evaluated using Stratified 5-Fold Cross-Validation, which preserves the original class distribution in each fold and provides a robust estimate of model performance.

5. Results and discussion

5.1. Time domain analysis

Figure 3 shows the time-domain responses of three sensors: acoustic (blue), vibration (green) and UVA (red), and under changing welding conditions. It shows how the welding UVA, vibration, and speed affect the signal characteristics. The test images at the bottom of each subplot show the physical welding results, helping to correlate signal variations with weld quality.

In subplot (a), with welding parameters of 275 A, 31.3 V, and 1.05m/s, the acoustic signal shows high amplitude with sharp drops, the vibration signal remains mostly stable with minor fluctuations, and the UVA signal displays frequent peaks, indicating arc instability. In subplot (b), at 245 A, 29.3 V, and 0.7m/min, the acoustic signal is low and steady, the vibration signal is stable, and the UVA signal gradually declines, reflecting consistent arc behaviour. These results highlight the sensitivity of acoustic, vibration, and UVA signals to current and voltage changes, supporting real-time weld quality monitoring.

5.2. Analysis of wavelet scattering features for sensor data

The wavelet scattering coefficients extracted from acoustic, vibration, and ultraviolet-A (UVA) sensors provide distinctive signatures of welding process stability, as illustrated in Figures 4(a) and (b).
Figures 4(a) show more dynamic scattering activity with increased intensity. Acoustic signals exhibit pronounced peaks, indicating arc instability. Vibration signals remain consistent but spatially uniform, suggesting mechanical disturbances. UVA signals fluctuate sharply, reflecting variations likely caused by oxidation or spatter.

In contrast, Figures 4(b) display low, stable intensity across all signals, indicating minimal process variation, steady arc behaviour, and a clean weld pool.

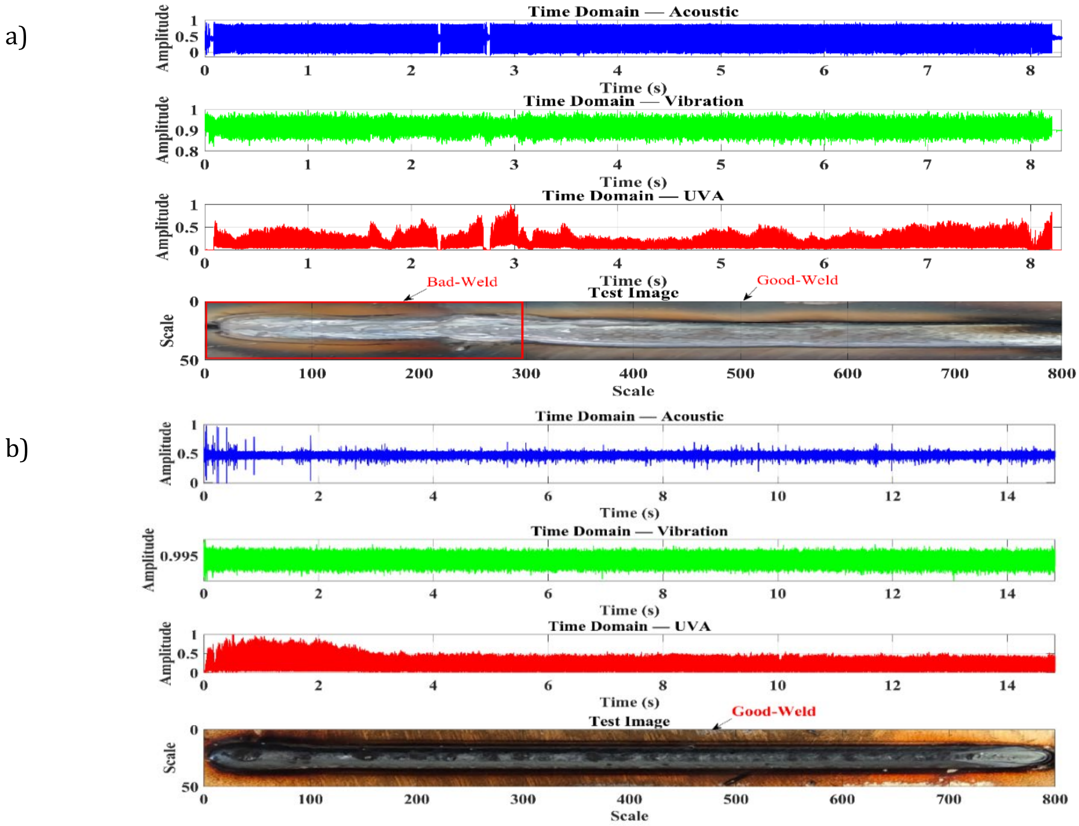

Figure 3. Time domain responses of acoustic, vibration, and UVA for (a) $I = 275$ [A], V =31.3 [V], and (b) $I = 245$ [A], $V = 29.3$ [V].

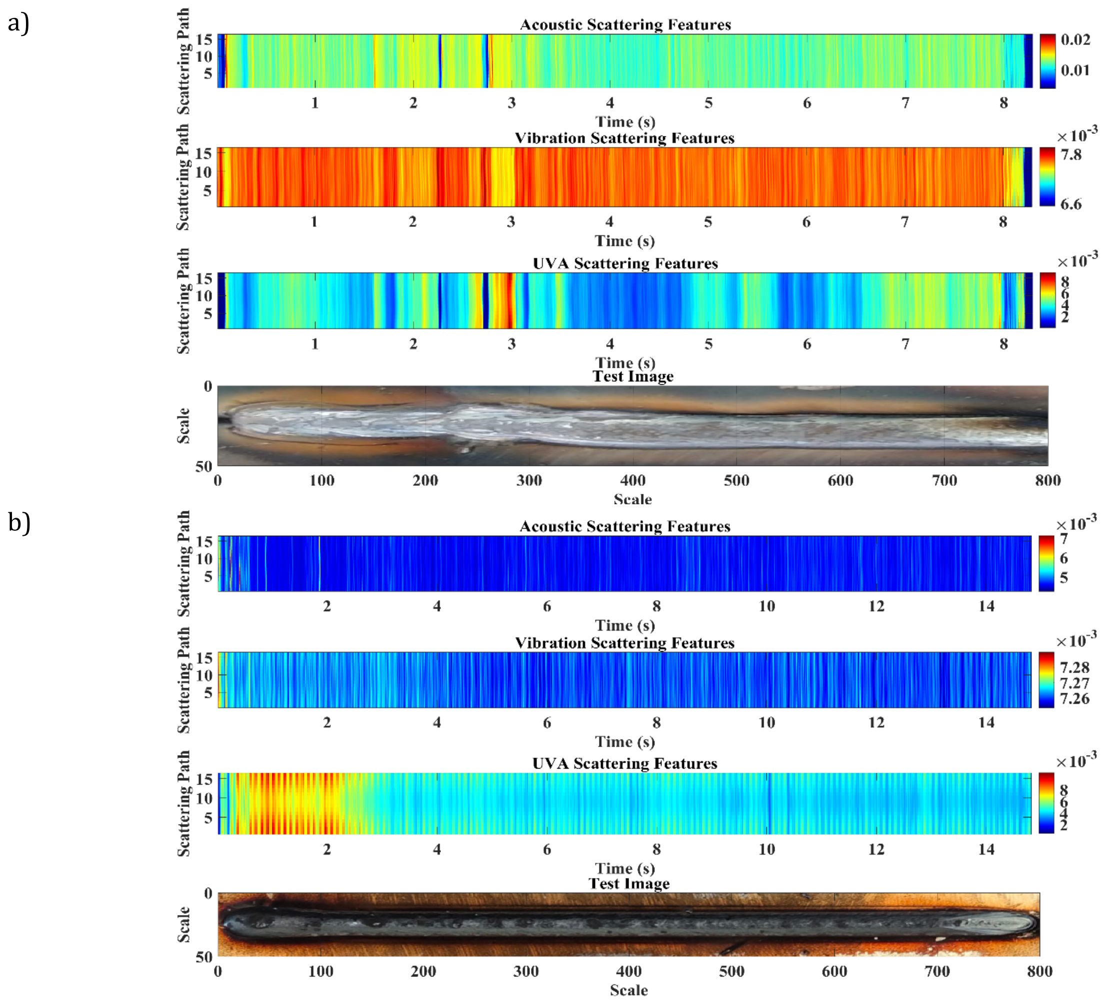

Figure 4. Wavelet scattering feature responses of acoustic, vibration, and UVA signals for (a) $I = 275$ [A], $V = 31.3$ [V] and (b) $I = 245$ [A], $V = 29.3$ [V].

5.3. Deep Autoencoder Model training and evaluation

The deep autoencoder configuration, illustrated in Figure 2 and detailed in Table 3, was trained on standardized scattering coefficients from defect-free samples to learn normal operational patterns. MSE was used to identify anomalies, with the detection threshold optimized on the validation set by maximizing the F1 score. The model's performance was evaluated on the test set using precision, recall, F1-score, accuracy, Receiver Operating Characteristic Area Under the Curve (ROC AUC), and confusion matrices.

The training history in Figure 5(a) demonstrates effective learning over 500 epochs, with steadily decreasing training and validation losses and no evidence of overfitting, while Figure 5(b) illustrates the precision–recall analysis together with the F1 score curve, revealing an optimal decision threshold of 0.2895 that maximizes the F1 score and provides a balanced trade-off between precision and recall.

In the first case Figure 6(a), the reconstructed signal aligns closely with the original, as indicated by a low MSE of 0.2673. This sample corresponds to a clean good weld and is therefore correctly classified as Normal. In contrast, the second case Figure 6(b) shows greater deviation and a higher MSE of 0.2877. This Partial weld contains both intact and defective transitions, making its classification sensitive to the MSE threshold. When defective segments dominate, the weld is classified as Defective, whereas cases in which intact segments prevail, as in Figure 6(c), are classified as Defective. Finally, the Bad weld shown in Figure 6(d) exhibits substantial reconstruction error, resulting in its accurate classification as Defective.

The scatter plots in Figure 7(a) illustrate how well the autoencoder reconstructs inputs by plotting density against reconstruction loss. Samples are labeled as Good, Partial, or Bad using the optimal threshold. Figure 7(b) applies the same threshold to classify samples as Predicted Normal or Predicted Defective based on MSE. These plots facilitate anomaly detection and allow assessment of model performance.

The model demonstrates strong performance in welding defect detection, achieving a ROC AUC of 99.7%, as shown in Figures 8(a) and 8(b). It attains 98.1% accuracy, 96.7% recall, and a 97.5% F1 score, indicating balanced and reliable classification. The confusion matrix in Figure 8(c) shows 99% specificity and 96.7% sensitivity, with low false positive (1%) and false negative (3.3%) rates.

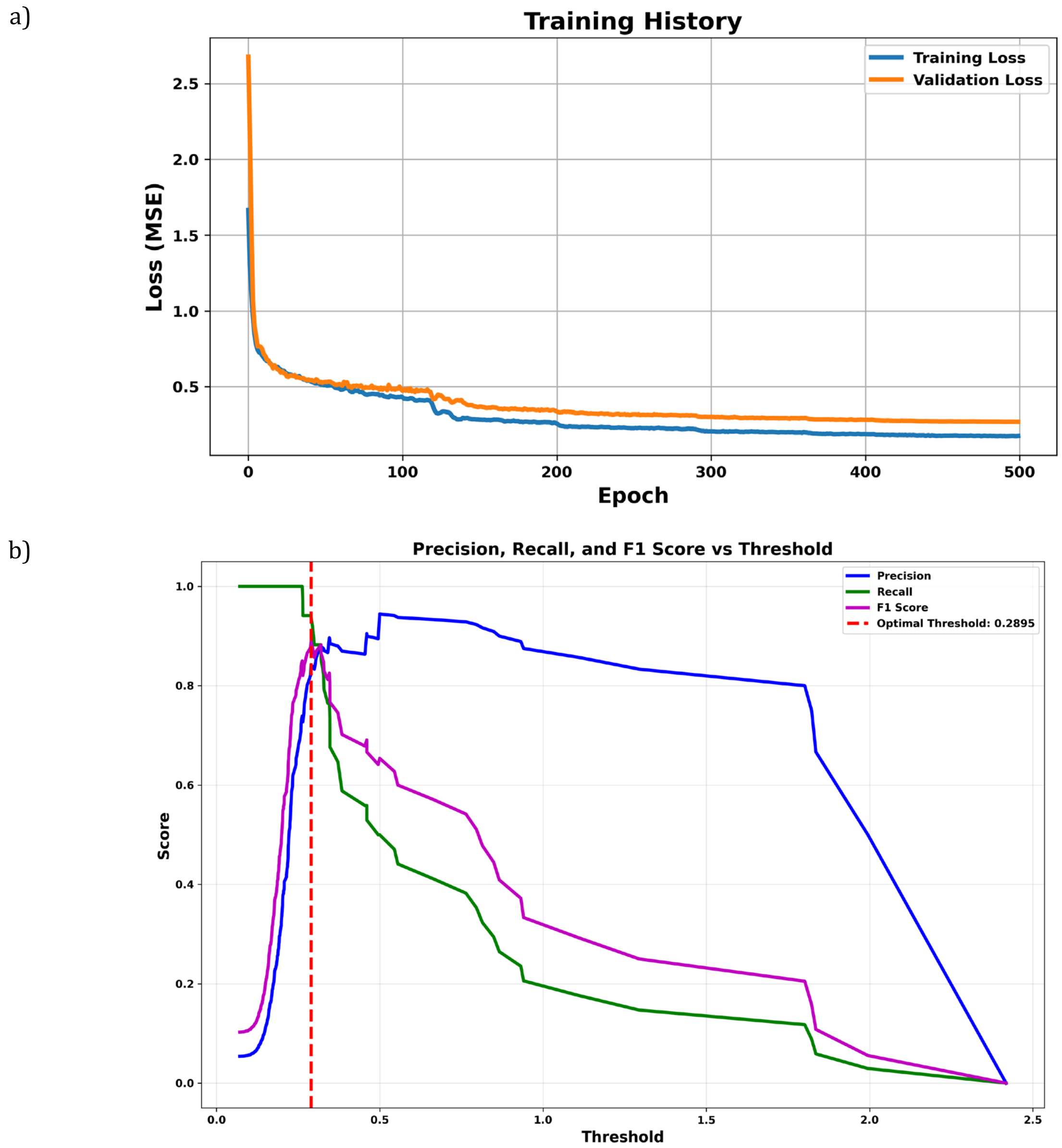

Figure 5. (a) Training and validation loss curves based on MSE. (b) Precision–recall analysis with F1score curve used for optimal threshold selection.

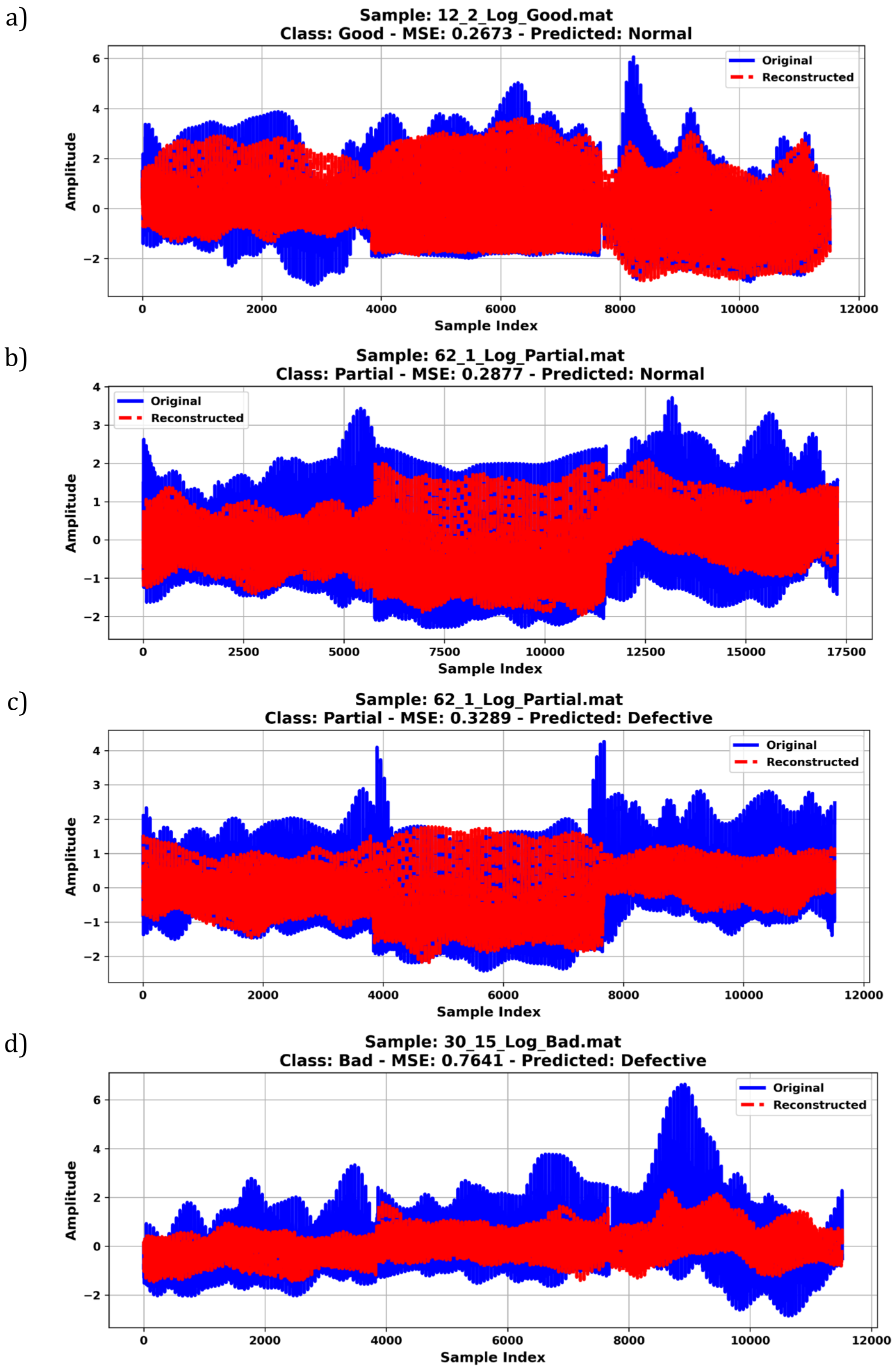

Figure 6. (a) Sample from the Good class. (b) Sample from the Partial class dominated by bad weld. (c) Sample from the Partial class dominated by good weld. (d) Sample from the Bad class.

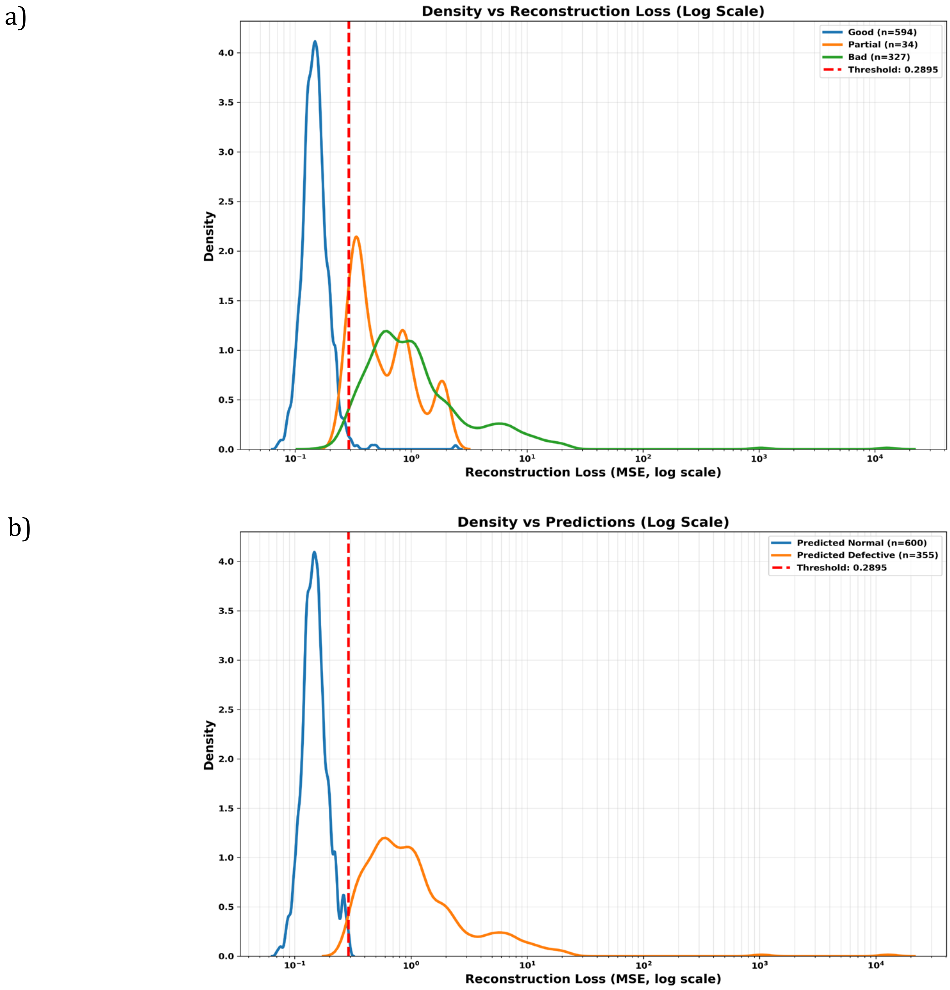

Figure 7. (a) Density vs reconstruction loss; (b) Density vs prediction.

The wavelet scattering-based defect detection model was evaluated for varying wavelet resolution Q and temporal averaging T. As shown in Table 1, optimal performance occurred at Q=2, yielding the highest evaluation metrics. Increasing Q to 4 slightly reduced performance and further increases to 8–12 caused minor declines, reflecting a trade-off between spectral resolution and sensitivity to brief anomalies.

Table 2 shows that a small averaging window (T=0.01 s) favors short-term defect detection, while larger values of T smooth the signal. This smoothing slightly improves recall but reduces accuracy. At T=0.03 s, the model achieved an accuracy of 95.5% and a recall of 88.4%. These results indicate that shorter averaging is more sensitive to transient defects.

Table 1. Impact of scattering parameters on deep autoencoder performance (T = 0.01 s).

Metric(%)	Q=2	Q=4	Q=8	Q=12
Accuracy	98.1	97.7	97.3	97.0
Precision	98.3	98.6	96.1	97.7
Recall	96.7	95.3	96.7	94.5
F1 Score	97.5	96.9	96.4	96.1
ROC AUC	99.7	99.6	99.2	99.1

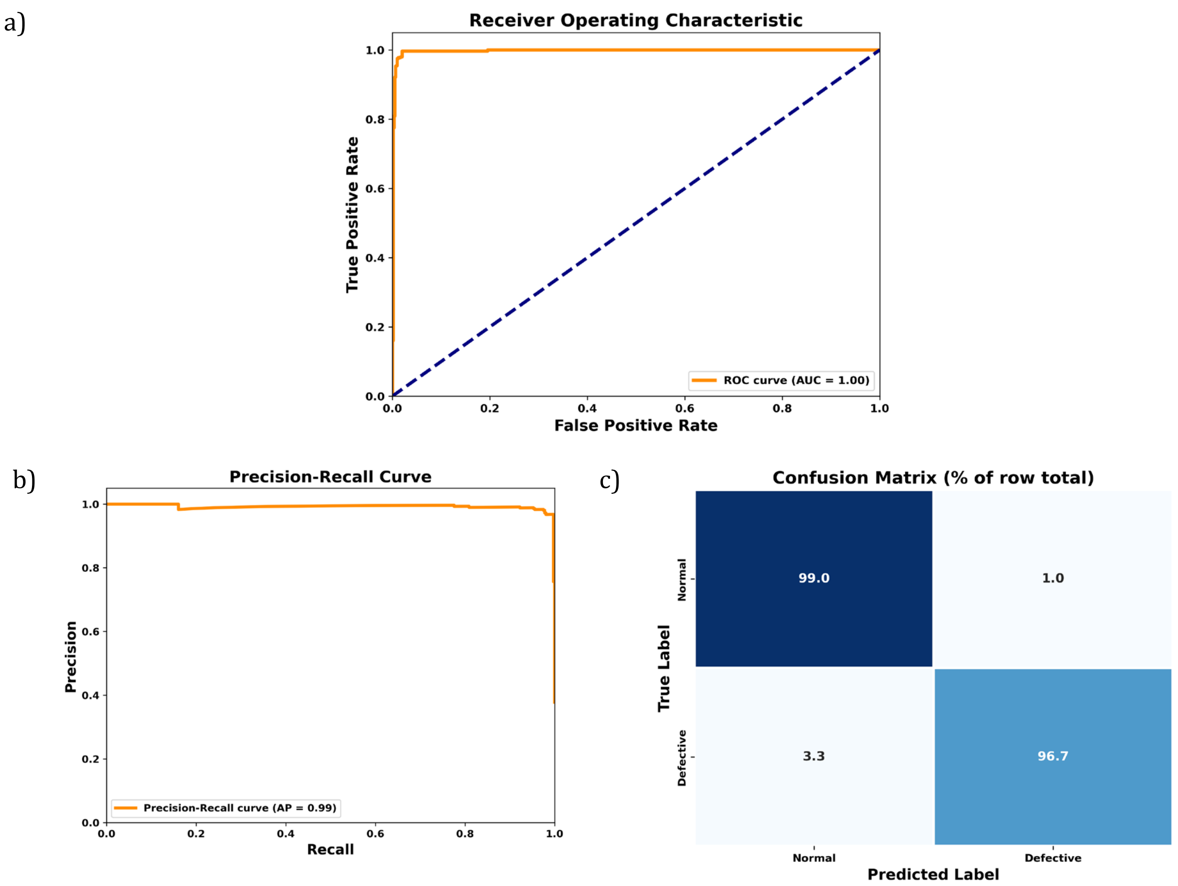

Figure 8. (a) Receiver Operating Characteristic curve, (b) Precision-Recall curve, (c) Confusion Matrix.

Table 2. Deep autoencoder performance for varying temporal averaging T [s] with $Q = 2$.

Metric (%)	T=0.01	T=0.02	T=0.03
Accuracy	98.1	98.1	95.5
Precision	98.3	98.0	99.7
Recall	96.7	96.9	88.4
F1 Score	97.5	97.5	93.7
ROC AUC	99.7	99.6	99.6

Table 3. Architecture of the Deep Autoencoder model.

Layer	Details
Input	Input layer (Dim = Number of Features)
1	Dense (512), ELU activation, L2 regularization (1e-4), Batch Normalization, Dropout (0.4)
2	Dense (256), ELU activation, L2 regularization (1e-4), Batch Normalization, Dropout (0.3)
3	Dense (256), ELU activation, L2 regularization (1e-4), Batch Normalization, Dropout (0.2)
4	Bottleneck: Dense (32), Linear activation
5	Dense (128), ELU activation, Batch Normalization
6	Dense (256), ELU activation, Batch Normalization
7	Dense (512), ELU activation, Batch Normalization
Output	Dense (Dim = Number of Features), Linear activation
Training Configuration	
Optimizer	Adam (learning rate = 0.001, clipvalue = 0.5)
Loss Function	MSE
Callbacks	EarlyStopping, ReduceLROnPlateau, ModelCheckpoint

Table 3 shows the architecture of the autoencoder. The evaluation of the three neural network architectures indicates that the model with 512 neurons per layer and dropout rates of 0.4, 0.3, and 0.2 achieves the strongest overall performance, with an F1 score of 97.5%, precision of 98.3%, recall of 96.7%, and a ROC AUC of 99.7%. The architecture with 256 neurons per layer demonstrates reduced performance, with an F1 score of 88.8%, precision of 99.3%, recall of 80.3%, and a ROC AUC of 98.3%. The smallest architecture, with 128 neurons per layer and dropout rates of 0.3, 0.2, and 0.1, exhibits the lowest performance, achieving an F1 score of 76.7%, precision of 99.1%, recall of 62.6%, and a ROC AUC of 95.5%. These results confirm that larger architectures with appropriate regularization provide stronger and more consistent performance across F1 score, precision, recall, and ROC AUC.

The results in Table 4 indicate that SVM and 1D CNN exhibit substantial performance improvements when SMOTE is applied to mitigate class imbalance. Without SMOTE, both models achieve lower accuracy, F1-score, and ROC AUC, highlighting their sensitivity to imbalanced data. In contrast, the unsupervised deep autoencoder attains the highest overall performance in terms of accuracy, F1-score, and ROC AUC without requiring labeled minority samples or any class balancing. These findings demonstrate that, while supervised models benefit from synthetic oversampling, the deep autoencoder provides a robust and effective solution for defect detection in highly imbalanced welding signal datasets.

Table 4. Performance of SVM, 1D CNN, and Deep Autoencoder on imbalanced welding data.

Model	Balancing Strategy	Accuracy (%)	F1-Score (%)	ROC AUC (OvR%)
SVM	SMOTE	95.9	95.9	99.5
	Original data	87.5	86.0	94.0
1D CNN	Original data	87.5	87.4	95.0
	SMOTE	96.9	96.9	99.9
Deep autoencoder	-	98.1	98.3	99.7

6. Conclusion

This work presents an unsupervised deep autoencoder for welding defect detection using wavelet scattering features and MSE loss. The proposed architecture, employing a deep network with appropriate regularization and dropout, consistently outperformed smaller variants, demonstrating greater robustness and generalization across varying temporal averaging settings. Unlike supervised models such as SVM and 1D CNN, which require data balancing to handle class imbalance, the autoencoder effectively detects defects without labeled data, providing a reliable and scalable solution for defect detection in highly imbalanced welding datasets.

6.1. Limitations

The proposed system has been evaluated exclusively in offline settings, and its performance in real-time MAG welding environments remains unverified. While the unsupervised autoencoder operates effectively without balanced datasets, supervised learning approaches remain dependent on class-balanced data to achieve optimal performance. Additionally, the model relies on high-quality and consistent MAG welding signals, which may limit its generalizability to other welding processes, alternative sensor configurations.

Author Contributions

All authors participated in the conceptualization and design of the manuscript. All authors have reviewed and approved the final version of the manuscript for publication.

Additional information

The author(s) declare: no competing financial interests and that all material taken from other sources (including their own published works) is clearly cited and that appropriate permits are obtained.

References

1. S. Luo, X. Ma, J. Xu, M. Li, L. Cao; Deep learning-based monitoring of spatter behavior by the acoustic signal in selective laser melting; Sensors, 2021, 21(21), 7179; DOI:10.3390/s21217179
2. D. Wu, P. Zhang, Z. Yu, Y. Gao et.al.; Progress and perspectives of in-situ optical monitoring in laser beam welding: Sensing, characterization and modeling; Journal of Manufacturing Processes, 2022, 75, 767-791; DOI: 10.1016/j.jmapro.2022.01.044

3. S. Kumari, R. Jain, U. Kumar, et.al.; Defect identification in friction stir welding using continuous wavelet transform; Journal of Intelligent Manufacturing, 2019, 30, 483-494; DOI: 10.1007/s10845-016-1259-1
4. V. Kumar, S. Ghosh, M. K. Parida, S. K. Albert; Application of continuous wavelet transform based on Fast Fourier transform for the quality analysis of arc welding process; International Journal of System Assurance Engineering and Management, 2024, 15(3), 917-930; DOI :10.1007/s13198-023-02178-7
5. E. C. Ozkat; Photodiode signal patterns: Unsupervised learning for laser weld defect analysis; Processes, 2025, 13(1), 121; DOI:10.3390/pr13010121
6. R. Mohandas, P. Mongan, M Hayes; Ultrasonic weld quality inspection involving strength prediction and defect detection in data-constrained training environments; Sensors, 2024, 24(20), 6553; DOI:10.3390/s24206553
7. V. Vasan, N.V. Sridharan, R. J. Balasundaram, S. Vaithiyanathan; Ensemble-based deep learning model for welding defect detection and classification; Engineering Applications of Artificial Intelligence, 2024, 136, 108961; DOI: 10.1016/j.engappai.2024.108961
8. D.-M. Tsai, P.-H Jen; Autoencoder-based anomaly detection for surface defect inspection; Advanced Engineering Informatics, 2021, 48, 101272; DOI: 10.1016/j.aei.2021.101272
9. K. Meyer, V Mahalec; Anomaly detection methods for infrequent failures in resistive steel welding; Journal of Manufacturing Processes, 2022, 75, 497-513; DOI: 10.1016/j.jmapro.2021.12.003
10. G. Mattera, J. Polden, J. Norrish; Monitoring the gas metal arc additive manufacturing process using unsupervised machine learning; Weld World, 2024, 68(11), 2853-2867; DOI:10.1007/s4019402401836z
11. J. Bruna, S. Mallat; Invariant scattering convolution networks; IEEE Transactions on Pattern Analysis and Machine Intelligence, 2013, 35(8), 1872-1886; DOI:10.1109/TPAMI.2012.230
12. I. D. Mienye, T. G. Swart; Deep Autoencoder Neural Networks: A Comprehensive Review and New Perspectives; Archives of Computational Methods in Engineering, 2025, 32, 3981–4000; DOI:10.1007/s11831-025-10260-5
13. J. Andén, S. Mallat; Deep scattering spectrum; IEEE Transactions on Signal Processing, 2014, 62(16), 4114-4128; DOI:10.1109/TSP.2014.2326991
14. Y. Sun, P. Bai, H. Sun, P. Zhou; Real-time automatic detection of weld defects in steel pipe; NDT & E International, 2005, 38(7), 522-528; DOI: 10.1016/j.ndteint.2005.01.011
15. L. Nele, G. Mattera, M. Vozza; Deep neural networks for defects detection in gas metal arc welding; Applied Sciences, 2022, 12(7), 3615; DOI:10.3390/app12073615
16. A. Ozga, M. Sulewski; Application of unsupervised learning algorithms for analysis the vibrations of an oscillator forced by a random series of impulses; Vibrations in Physical Systems, 2023, 34(1), 2023121; DOI:10.21008/j.0860-6897.2023.1.21
17. X. Zhu, A.E. Çetin; Efficient Bearing Sensor Data Compression via an Asymmetrical Autoencoder with a Lifting Wavelet Transform Layer; 2025 IEEE International Symposium on Circuits and Systems (ISCAS), 1-5; DOI:10.1109/ISCAS56072.2025.11043949
18. H. Zhang, Q. Wu, W. Tang, J. Yang; Acoustic signal-based defect identification for directed energy deposition-arc using wavelet time–frequency diagrams; Sensors, 2024, 24(13), 4397; DOI:10.3390/s24134397
19. D. Kumar, S. Azam, et al.; Clarity-Optimized Wavelet with Autoencoder-ReliefF Ranking for Enhanced UHF PD Signal Feature Extraction; IEEE Access, 2025, 13, 182444–182457; DOI:10.1109/ACCESS.2025.3619762
20. K. Pal, S. Bhattacharya, S.K. Pal; Investigation on arc sound and metal transfer modes for on-line monitoring in pulsed gas metal arc welding; Journal of Materials Processing Technology, 2010, 210(10), 1397-1410; DOI: 10.1016/j.jmatprotec.2010.03.029
21. G. Zhang, G. He, Y. Gu, Y. Shi; Effect of process parameters on arc shape, macroscopic features, and microhardness in pulsed GMA additive manufacturing; Crystals, 2023, 13(3), 546; DOI:10.3390/cryst13030546
22. A. Klimpel; The physical and technological background of the GMA process; Japan Journal of Research, 2024, 5(2); DOI:10.33425/2690-8077.1106